Effects of nanoscale density inhomogeneities on shearing fluids

Benjamin A. Dalton* and Peter J. Daivis†
School of Applied Sciences, RMIT University, GPO Box 2476 Melbourne, Victoria 3001, Australia

J. S. Hansen
DNRF Centre Glass and Time, IMFUFA, Department of Sciences, Roskilde University, Postbox 260, DK-4000 Roskilde, Denmark

B. D. Todd
Mathematics, Faculty of Engineering and Industrial Sciences, and Centre for Molecular Simulation, Swinburne University of Technology, P.O. Box 218, Hawthorn, Victoria 3122, Australia

(Received 24 September 2013; published 27 November 2013)

It is well known that density inhomogeneities at the solid-liquid interface can have a strong effect on the velocity profile of a nanoconfined fluid in planar Poiseuille flow. However, it is difficult to control the density inhomogeneities induced by solid walls, making this type of system unsuitable for a comprehensive study of the effect on density inhomogeneity on nanofluidic flow. In this paper, we employ an external force compatible with periodic boundary conditions to induce the density variation, which greatly simplifies the problem when compared to flow in nonperiodic nanoconfined systems. Using the sinusoidal transverse force method to produce shearing velocity profiles and the sinusoidal longitudinal force method to produce inhomogeneous density profiles, we are able to observe the interactions between the two property inhomogeneities at the level of individual Fourier components. This gives us a method for direct measurement of the coupling between the density and velocity fields and allows us to introduce various feedback control mechanisms which customize fluid behavior in individual Fourier components. We briefly discuss the role of temperature inhomogeneity and consider whether local thermal expansion due to nonuniform viscous heating is sufficient to account for shear-induced density inhomogeneities. We also consider the local Newtonian constitutive relation relating the shear stress to the velocity gradient and show that the local model breaks down for sufficiently large density inhomogeneities over atomic length scales.

DOI: 10.1103/PhysRevE.88.052143 PACS number(s): 61.20.−p, 62.25.−g, 62.10.+s, 66.20.Cy

I. INTRODUCTION

At a fluid-solid interface a fluid will exhibit large spatial density oscillations that can extend up to 5 atomic diameters from the wall [1–3]. The magnitude of these oscillations decays as the distance from the wall increases. This effect is due to the geometric packing of the fluid atoms in the regions directly neighboring the wall and so the length of each oscillation cycle is generally of the order of a single atomic diameter. When a two-wall channel of width less than 10 atomic diameters is used to confine a fluid, then these large characteristic oscillations in the fluid density extend across the entire confining channel. The solution to the Navier-Stokes equation for the flow of a fluid confined between two parallel, planar walls, driven by a constant gravitational-like force in the direction parallel to the walls, is a quadratic velocity profile. However, it is well known that for atomic and molecular fluids confined between planar walls separated by less than 10 atomic diameters the field-induced velocity profile displays large oscillations superimposed onto the underlying quadratic profile [2–4]. These variations in the velocity are spatially aligned with the oscillations in the density. Under the influence of such density inhomogeneities the velocity profiles can exhibit multiple gradient inflections and, in extreme cases, even gradient reversals [2].

The currently available theoretical methods to predict the velocity profile in a flowing nanoconfined fluid fall into two categories. One approach is to use kinetic theory. The modified Enskog theory of Davis and co-workers [5–7], as well as the approach using the generalized Langevin equation of Pozhar *et al*. [8–10], provide rigorous results for simple atomic systems such as the hard sphere fluid, but are complicated and difficult to extend to more complex fluids. Guo *et al*. [11,12] have proposed a generalized hydrodynamic model derived from a simplified Enskog-like kinetic theory. Their approach is also currently only applicable to simple atomic fluids and it is limited to isothermal systems. More recently Marconi and Melchionna have described a dynamic density functional theory based on a combination of kinetic and density functional theories, which has not yet been applied to transport in strongly inhomogeneous fluids but is promising in that it can, in principle, be applied to complex fluids such as colloids and molecular fluids [13].

The other common approach is the local average density model (LADM) of Bitsanis *et al*., which accounts for the nonlocal dependence of the viscosity on the density [14,15]. Rather than the viscosity at a point depending on the density at that point, in the LADM it depends on the average density taken in a spherical volume around that point. Hoang and Galliero [16–18] extended the method by investigating various weighting functions to scale the contribution of the density throughout the volume in the calculation of the average density at which the viscosity is evaluated. Although the LADM can produce satisfactory results under some circumstances,

*Email address: benjamin.dalton@rmit.edu.au
†Email address: peter.daivis@rmit.edu.au

it has not been successful in predicting all characteristics of the velocity profile for the nanoconfined fluid such as the gradient reversals shown by Travis and Gubbins [2]. This failure is probably due to the neglect in the LADM of any nonlocal dependence of the stress on the velocity gradient. It is known that even for fluids with homogeneous density profiles the dependence of the shear stress on the velocity gradient is essentially nonlocal [19,20]. This nonlocal dependence becomes apparent when the gradient variations in the velocity profile are significant over length scales of the order of a few atomic diameters. Under these conditions it is appropriate to relate the shear stress to the strain rate via a nonlocal viscosity kernel. Cadusch *et al*. [21] showed that a translationally invariant nonlocal viscosity kernel can be used to approximate the position-dependent kernel in a confined fluid when the confinement channel is significantly wider then the kernel width. For highly confined fluids, where the density inhomogeneities are significant across the whole channel, the translationally invariant kernel is no longer adequate and the stress may depend nonlocally on both the strain rate and the density.

In this paper we present a simplified molecular dynamics (MD) simulation method which can be used to investigate shearing flow in fluids where the density varies strongly over nanoscopic length scales. We explore the proposed technique and describe how it can be implemented to produce various idealized inhomogeneous fluid systems. We discuss the results in the context of nanoconfined fluids.

The approach we describe uses a combination of two spatially sinusoidally varying external fields that act as body forces on the atoms in an unconfined, simple atomic fluid. The first external field is a sinusoidal transverse force (STF), which shears the fluid. The STF method is a classic technique in the study of nonequilibrium and shearing steady states and was one of the first methods used to compute the shear viscosity using nonequilibrium MD methods as an alternative to the equilibrium Green-Kubo approach [22]. The STF method has been used to study shear-induced heat flow in systems with homogeneous temperature profiles [23], the wave vector and strain rate dependence of shear viscosity [24], and the nonlocal dependence of shear stress on strain rate [19,20,25]. It has been shown that the velocity profiles induced by the STF method induce density perturbations in the shearing fluid due to nonuniform viscous dissipation and thermal expansion [23]. In general, STF investigations have been restricted to the small field regime where it is known that density perturbations are negligible. Therefore, the use of this technique for studying shearing fluids with strongly inhomogeneous densities has so far been avoided. In addition to the STF we implement a sinusoidal longitudinal force (SLF). In a recent publication we used the SLF method to investigate the linear and nonlinear density response functions for simple atomic fluids [26]. We developed a method for systematically perturbing fluid densities and measuring the Fourier components of the inhomogeneous density profiles. We determined the full response relationship between single Fourier component SLFs and cosine series inhomogeneous density profiles and described in detail the manifestation of the nonlinear density response as higher-order cosine harmonics.

In the present paper we combine the STF and SLF methods to investigate the effects of cosine series density perturbations in sinusoidal series velocity profiles. The combined STF-SLF method enables us to investigate the interactions between the density and velocity inhomogeneities at the level of individual Fourier components. This greatly simplifies the problem of inhomogeneous shearing fluids when compared to the flowing confined fluid where the density profile is a response of the total fluid-solid system, which cannot be easily controlled. In addition, we show how a constraint mechanism can be used to fix individual Fourier components of the density, allowing us to completely eliminate density inhomogeneity or fix it in a controllable way. Although the method is synthetic, in that it uses external fields to perturb unconfined fluids that satisfy periodic boundary conditions, it can be used to isolate characteristics of the strongly inhomogeneous flow that are very difficult to isolate in the more realistic confined system. This deconstructive ability of the method makes it especially useful for empirically determining response functions characteristic of a fluid, which can then be used to predict the behavior of the fluid under realistic confinement conditions.

The outline of this paper is as follows. First we summarize the necessary theoretical description of the fluid properties of shearing inhomogeneous fluids and describe the MD simulation method used to generate our results. In the results section we investigate shear-induced density perturbation and we consider the role of homogeneous and inhomogeneous temperature profiles. We then introduce the SLF and observe the effects of both long and short wavelength density inhomogeneities in shearing flow. Finally we use a combination of multiple density cosine components to produce pseudo-channel-like density profiles and observe their effects on the velocity profiles.

II. MD SIMULATIONS OF AN ATOMIC FLUID UNDER STF AND SLF

A. Properties of the STF-SLF fluid

We consider an unconfined, simple atomic fluid with periodic boundary conditions under the influence of two spatially sinusoidally varying external forces, where both forces are constant in time. The first force is the STF [22,23,25]. The STF is a body force acting in the x direction on each atom of a fluid, with a magnitude that is a sinusoidal function of the atom's position in the y dimension. The STF is given by

$$\mathbf{F}^t(y) = F_0^t \sin(k_n y)\mathbf{i}, \tag{1}$$

where F_0^t is the force amplitude, $k_n = 2\pi n/l_y$ is the force wave number for positive integers n, l_y is the length of the MD simulation space in the y dimension, and $\mathbf{i}$ is the unit vector in the x direction. The direction of the force is transverse to the direction in which the force magnitude varies and so the effect of the STF on the fluid is to produce inhomogeneous shearing flow in the x direction.

The second force is the SLF. This force is equivalent to the sinusoidally varying potential (SVP) of Hoang and Galliero [16]. The SLF is a body force acting on each atom in the y direction with a magnitude that is also a function of an atom's

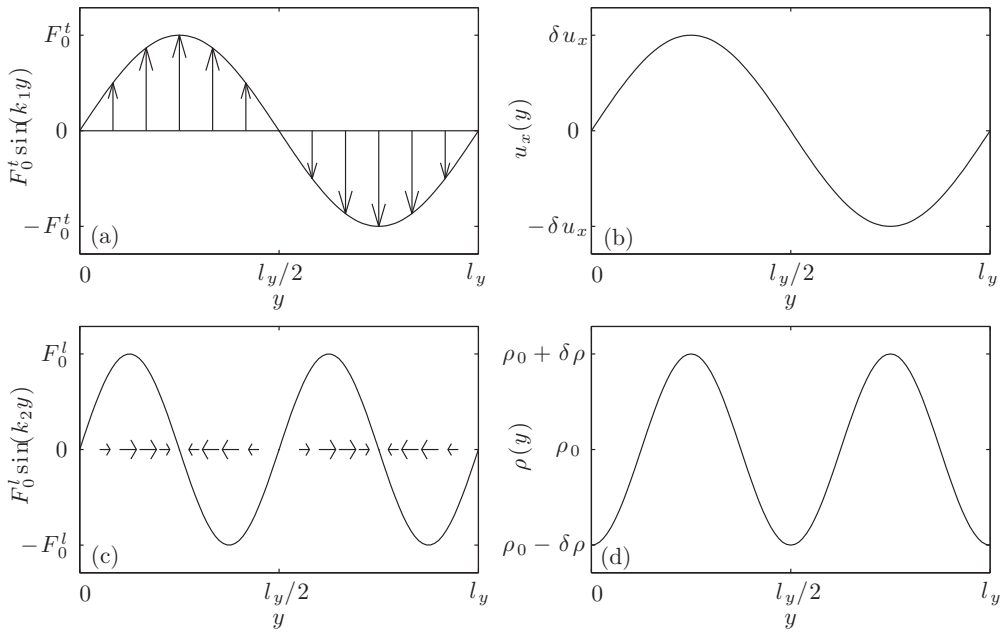

FIG. 1. (a) STF for $n = 1$ applied in the x direction. (b) x component of the streaming velocity profile due to the STF. (c) SLF for $m = 2$ applied in the y direction. (d) Inhomogeneous density profile due to SLF.

position in the y dimension. The SLF is given by

$$\mathbf{F}^l(y) = F_0^l \sin(k_m y)\mathbf{j}, \tag{2}$$

where F_0^l is the force amplitude, $k_m = 2\pi m/l_y$ is the force wave number for any positive integer m, and $\mathbf{j}$ is the unit vector in the y direction. The SLF produces static average density perturbations in a fluid. We have described the density response of a fluid due to the SLF in detail in a recent publication [26]. The force is intentionally chosen to be in the y direction so that we can produce inhomogeneous density profiles that vary in the same direction that the velocity profiles vary.

Since the STF is applied in the x direction only, for low Reynolds number we expect the streaming velocity to have an x component only. The most general form of the x component of the streaming velocity of a fluid with periodic boundary conditions under the influence of the two forces just described will be a sinusoidal series,

$$u_x(y) = \sum_{p=1}^{\infty} u_{xp} \sin(k_p y). \tag{3}$$

Thus, u_{xp} is the coefficient of the pth term in the series for a streaming velocity profile for the fluid flowing in the x direction. In the steady state the corresponding strain rate $\dot{\gamma}(y) = du_x(y)/dy$ will be

$$\dot{\gamma}(y) = \sum_{p=1}^{\infty} k_p u_{xp} \cos(k_p y). \tag{4}$$

From the internal energy balance equation the temperature profile will be proportional to $\dot{\gamma}^2$. In general, we can write the temperature as an even cosine series,

$$T(y) = T_0 + \sum_{q=1}^{\infty} T_{2q} \cos(k_{2q} y), \tag{5}$$

where T_0 is the average temperature. The only assumption we make about the density is that it is symmetric about $l_y/2$; therefore,

$$\rho(y) = \rho_0 + \sum_{v=1}^{\infty} \rho_v \cos(k_v y), \tag{6}$$

where ρ_0 is the average density. The components of the density are free to respond to either the SLF, the shearing flow, or both.

Figure 1 shows (a) the STF and (c) the SLF given by Eqs. (1) and (2) for $n = 1$ and $m = 2$, respectively. The arrows are used to indicate the direction and magnitude of each force. Also shown is (b) the x component of the streaming velocity induced by the STF and (d) the inhomogeneous density profile induced by the SLF. The STF and induced velocity profile are both sinusoidal functions. The SLF is also a sinusoidal function but the SLF-induced density profile is cosinusoidal. The potential energy field associated with the conservative SLF is, however, cosinusoidal, which explains why the density profile is cosinusoidal [26].

We can determine the yx component of the pressure tensor for a fluid under the influence of the two external fields using the momentum balance equation,

$$\frac{\partial \rho \mathbf{u}}{\partial t} = -\nabla \cdot \mathbf{P} + \rho \mathbf{F}^t - \nabla \cdot (\rho \mathbf{u}\mathbf{u}). \tag{7}$$

$\mathbf{P}$ is the pressure tensor, $\mathbf{u}$ is the streaming velocity and $\mathbf{F}^t$ is the STF. In the steady state we will have $\partial \rho \mathbf{u}/\partial t = 0$ and also $\nabla \cdot (\rho \mathbf{u}\mathbf{u}) = 0$, so $\nabla \cdot \mathbf{P} = \rho \mathbf{F}^t$. Since the STF is a force in the x direction and since the components of the pressure tensor are constant in the xz plane, Eq. (7) will reduce to $\partial P_{yx}(y)/\partial y = \rho(y) F_x^t(y)$. Integrating both sides between 0 and y, we obtain the y dependence

$$P_{yx}(y) = \int_0^y F_x^t(y')\rho(y')dy' + P_{yx}(0). \tag{8}$$

The SLF does not appear explicitly in Eq. (8) but is implicit in the density profile, which is given by Eq. (6). For a single sine component STF and general cosine series density, $P_{yx}(y)$ becomes

$$P_{yx}(y) = \rho_0 F_0^t \int_0^y \sin(k_n y')dy' + F_0^t \sum_{\upsilon=1}^{\infty} \rho_\upsilon \int_0^y \sin(k_n y')\cos(k_\upsilon y')dy' + P_{yx}(0). \tag{9}$$

Using the trigonometric identity $\sin(k_n y)\cos(k_\upsilon y) = \{\sin[(k_n + k_\upsilon)y] + \sin[(k_n - k_\upsilon)y]\}/2$ in Eq. (9), we obtain

$$P_{yx}(y) = -\frac{\rho_0 F_0^t}{k_n}\cos(k_n y) - \frac{\rho_0 F_0^t}{k_n} - \frac{F_0^t}{2}\sum_{\upsilon=1}^{\infty}\left[\frac{\rho_\upsilon \cos(k_{n+\upsilon} y)}{k_{n+\upsilon}} + \frac{\rho_\upsilon \cos(k_{n-\upsilon} y)}{k_{n-\upsilon}}\right] - \frac{F_0^t}{2}\sum_{\upsilon=1}^{\infty}\left[\frac{\rho_\upsilon}{k_{n+\upsilon}} + \frac{\rho_\upsilon}{k_{n-\upsilon}}\right] + P_{yx}(0), \tag{10}$$

where $k_n + k_\upsilon \equiv k_{n+\upsilon}$ and $k_n - k_\upsilon \equiv k_{n-\upsilon}$. Due to the symmetry of the cosine function $k_{n-\upsilon}$ will be equivalent to $k_{|n-\upsilon|}$ to account for $\upsilon > n$. The series of constants in the last line of Eq. (10) are due to the evaluation of the cosine at $y' = 0$ in the definite integral. When n is odd and υ is even we can use $P_{yx}(l_y/4) = 0$ to show that the terms in the last line must cancel.

B. Equations of motion for the STF-SLF system

We wish to determine the classical equations of motion for a simple atomic fluid that includes the STF and SLF as body force terms, as well as two additional constraint mechanisms. The first constraint is the cosine Fourier component thermostat originally introduced by Baranyai *et al.* [23]. The thermostat allows us to control the cosine Fourier components that are excited in the temperature profile given in Eq. (5). The second constraint is a density constraint, which we will call a pycnostat. The pycnostat allows us to control the cosine Fourier components that are excited in the density profile given in Eq. (6).

We determine the equations of motion for the system using Gauss's principle of least constraint [27]. This requires us to propose a specific constraint equation for each individual constraint applied to the system. For the thermostat constraints we begin by defining the instantaneous local kinetic temperature in terms of the microscopic peculiar kinetic-energy density

$$T(y) = \frac{1}{gk_B A_y}\sum_{i=1}^{N}\frac{m_i}{\rho(y)}\left[\frac{\mathbf{p}_i}{m_i} - u_x(y)\mathbf{i}\right]^2\delta(y - y_i), \tag{11}$$

where g is the dimensionality of the system, k_B is Boltzmann's constant, and $A_y = l_x l_z$ is the area of the simulation cell normal to the y dimension which comes from an integration over the x and z dimensions to eliminate $\delta(x - x_i)$ and $\delta(z - z_i)$. The summation is over all N atoms in the system and i labels the ith atom. Since we are considering a periodic system the specific constraint equation for the thermostat used to control the υth cosine component of the temperature profile is given by the coefficient of the υth term in the Fourier series representation of Eq. (11), where the coefficients of the series are given by

$$T_\upsilon^0 = \frac{2}{gk_B V}\int\sum_{i=1}^{N}\frac{m_i}{\rho(y)}\left[\frac{\mathbf{p}_i}{m_i} - u_x(y)\mathbf{i}\right]^2 \times \delta(y - y_i)\cos(k_\upsilon y)dy = \frac{2}{gk_B V}\sum_{i=1}^{N}\frac{m_i}{\rho(y_i)}\left[\frac{\mathbf{p}_i}{m_i} - u_x(y_i)\mathbf{i}\right]^2\cos(k_\upsilon y_i). \tag{12}$$

The factor of 2 and l_y implied in the volume is from the definition of the Fourier coefficient for a Fourier series. T_υ^0 represents the target value for the Fourier component thermostat with wave number $k_\upsilon = 2\pi\upsilon/l_y$ for any $\upsilon = 0,1,2,\ldots$. The unique index υ labels the constrained components of the temperature and can be chosen arbitrarily. T_υ^0 can be either zero or nonzero since the thermostat can be used to either suppress or induce temperature inhomogeneities. It should be noted that by setting $\upsilon = 2p$, where p is the index used for the velocity series Eq. (3), and $T_\upsilon^0 = T_{2p}^0 = 0$, we can maintain a homogeneous temperature profile for a system under STF.

For the pycnostat constraint we define the y-dependent microscopic density as

$$\rho(y) = \frac{1}{A_y}\sum_{i=1}^{N} m_i\delta(y - y_i). \tag{13}$$

The constraint equation for each pycnostat constraint term is given by setting the coefficient for the μth term in the Fourier series representation of Eq. (13) to a constant value,

$$\rho_\mu^0 = \frac{2}{V}\int\sum_{i=1}^{N} m_i\delta(y - y_i)\cos(k_\mu y)dy = \frac{2}{V}\sum_{i=1}^{N} m_i\cos(k_\mu y_i), \tag{14}$$

where ρ_μ^0 is the target value for the pycnostat with wave number $k_\mu = 2\pi\mu/l_y$ for any $\mu = 1,2,3,\ldots$. μ, therefore, labels the constrained components of the density profile.

To apply Gauss's principle of least constraint, we must express the constraint equations Eqs. (12) and (14) in an acceleration dependent form. $dT_\upsilon^0/dt = 0$ provides the acceleration-dependent form of the temperature constraint equation. The acceleration-dependent form of the density constraint equation is given by $d^2\rho_\mu^0/dt^2 = 0$. We introduce the square of the curvature $C(\ddot{\mathbf{r}}^N) = (1/2)\sum_{i=1}^{N} m_i(\ddot{\mathbf{r}}_i - \mathbf{F}_i/m_i)^2$, where $\ddot{\mathbf{r}}^N = (\ddot{\mathbf{r}}_1,\ddot{\mathbf{r}}_2,\ldots,\ddot{\mathbf{r}}_N)$ is the vector of particle accelerations and $\mathbf{F}_i$ is the total force acting on the ith atom. If $\mathbf{F}_i^\phi$ is the force on atom i due to all interatomic interactions then the total force acting on the ith atom will be $\mathbf{F}_i = \mathbf{F}_i^\phi + \mathbf{F}_i^t + \mathbf{F}_i^l$, where $\mathbf{F}^t$ and $\mathbf{F}^l$ are the STF and SLF given by Eqs. (1) and (2), respectively. Gauss's principle states that the actual motion of the system will be that which satisfies the following minimization with

respect to individual atomic accelerations

$$\frac{\partial}{\partial \ddot{\mathbf{r}}^N}\left[\frac{1}{2}\sum_{i=1}^{N} m_i\left(\ddot{\mathbf{r}}_i - \frac{\mathbf{F}_i}{m_i}\right)^2 - \sum_{\upsilon}\alpha_\upsilon \frac{dT_\upsilon^0}{dt} - \sum_{\mu}\beta_\mu \frac{d^2\rho_\mu^0}{dt^2}\right] = 0, \tag{15}$$

where α_υ and β_μ are the Gaussian scalar constraint multipliers. There will be one unique constraint multiplier for each constraint included. Thus, the summations over υ and μ are over all arbitrarily selected components of the thermostat and pycnostat, respectively.

Since $\partial/\partial\ddot{\mathbf{r}}^N$ is a vector we lose the summation over i and gain a system of $3N$ second-order differential equations. By defining $\dot{\mathbf{r}}_i = \mathbf{p}_i/m_i$ we obtain the following system of $6N$ first-order equations of motion:

$$\dot{\mathbf{r}}_i = \frac{\mathbf{p}_i}{m}, \quad \dot{\mathbf{p}}_i = \mathbf{F}^\phi + F_0^t \sin(k_n y_i)\mathbf{i} + F_0^l \sin(k_m y_i)\mathbf{j} - \frac{2}{gk_B}\left[\frac{\alpha_0}{\rho(y_i)} + \sum_{\upsilon}\frac{\alpha_\upsilon}{\rho(y_i)}\cos(k_\upsilon y_i)\right][\mathbf{p}_i - mu_x(y_i)\mathbf{i}] - \sum_{\mu}\beta_\mu k_\mu \sin(k_\mu y_i)\mathbf{j}. \tag{16}$$

We have separated the thermostat into two terms to distinguish the zero-wave-vector component with multiplier α_0, which is used to keep the average temperature of the whole system at a constant value.

To determine the thermostat multipliers we use a Nosé-Hoover integral feedback approach [28–30]. For each thermostat multiplier we introduce an additional degree of freedom to the system and hence solve the following additional equation of motion:

$$\dot{\alpha}_\upsilon = \frac{T_\upsilon - T_\upsilon^0}{\zeta_\upsilon}. \tag{17}$$

T_υ represents the calculated instantaneous value of the υth Fourier coefficient of the temperature profile. T_υ^0 is the target value for the coefficient described above, which we choose as an input parameter for each thermostat component. For the average temperature of the whole system we select the zero-wave-vector temperature target value T_0^0 and calculate T_0 at each instant using Eq. (12) with $\upsilon = 0$. The ζ_υ is chosen for each constraint and is used to vary the rigidity of the feedback.

We use two methods to evaluate the β_μ multipliers. The first is a Nosé-Hoover-type integral feedback analogous to Eq. (17),

$$\dot{\beta}_\mu = \frac{\rho_\mu - \rho_\mu^0}{\xi_\mu}, \tag{18}$$

where ρ_μ is the measured instantaneous value of the μth coefficient, ρ_μ^0 is the target value, and ξ_μ is the feedback constant. The second method is a proportional feedback method analogous to the Berendsen thermostat [31], where

$$\beta_\mu = \frac{\rho_\mu - \rho_\mu^0}{\xi_\mu}. \tag{19}$$

Using Eq. (19) has the disadvantage that it is not reversible but it has the advantage that it can provide a greater rigidity within the bounds of the numerical stability of the MD integrator algorithm. As we show in the Results section, we quite often require the pycnostat to suppress or induce large perturbations in the density. We found through experience that for the most extreme perturbations it was the Berendsen type pycnostat employing Eq. (19) that was most able to ensure numerical stability. The value of ξ_μ could obviously be varied to provide greater damping, but the stability of the MD algorithm is limited as $\xi_\mu \to 0$. Thus, for the possible values of ξ_μ we found that Eq. (19) was able to provide the density constraints for the largest perturbations, while Eq. (18) would quite often fail to provide numerical stability. For consistency, all results presented in this paper were obtained using Eq. (19).

The methods for calculating the Fourier coefficients of the velocity and temperature series and the density series have been described in detail in previous publications [23,26]. For the streaming velocity series coefficients, a system of linear equations is constructed by minimizing the sum of the squares of the differences between the instantaneous x direction total velocities of each atom and a proposed general sine series as a function of each atom's y position. At each time step the linear system is solved to evaluate the coefficients for the proposed sine series. The coefficients for the temperature series are calculated in the same manner, whereas now we use the instantaneous peculiar kinetic-energy density, Eq. (11). To determine the coefficients for the density series we use a direct microscopic Fourier decomposition of the instantaneous atomic positions. For each wavelength we determine the corresponding coefficient by $\rho_\upsilon = (2/V)\sum_{i=1}^{N} m_i \cos(k_\upsilon y_i)$, where V is the volume of the simulation cell and the factor of 2 accounts for the symmetry of the cosine function with respect to positive and negative values of k (see also [32]). All y-dependent density, temperature, and velocity profiles presented in this paper are Fourier series reconstructions using the time averaged coefficients. The results should not be confused with histogram representations.

III. SIMULATION DETAILS

For all simulations we use $N = 1372$ single component atoms, where the atoms interact using a truncated and shifted Lennard-Jones potential energy function, generally referred to as the WCA potential [33],

$$\phi(r_{ij}) = \begin{cases} 4\epsilon\left[\left(\frac{\sigma}{r_{ij}}\right)^{12} - \left(\frac{\sigma}{r_{ij}}\right)^{6}\right] + \epsilon, & r_{ij} \leqslant 2^{1/6}\sigma, \\ 0, & r_{ij} > 2^{1/6}\sigma, \end{cases} \tag{20}$$

where r_{ij} is the separation between the ith and jth atoms, ϵ represents the potential well depth, and σ is the separation at which the potential energy function is zero. All simulations are performed at a single state point with a constant reduced average temperature of $T_0 = 0.765$ and reduced average density $\rho_0 = 0.685$. The reduced temperature is determined by $T_0 = k_B T/\epsilon$ and the reduced density is $\rho_0 = \rho\sigma^3$. In reduced units all atoms have identical mass $m_i = 1.0$. Each system is prepared from a $7 \times 7 \times 7$ unit cell FCC crystal state and the cubic simulation cell has equal side lengths $l_x = l_y = l_z = 12.605$. Periodic boundary conditions are used in all three dimensions. The Gear predictor-corrector algorithm

TABLE I. A summary of all simulations discussed in this paper. F_0^t is the amplitude of the STF, Eq. (1) and F_0^l is the amplitude of the SLF, Eq. (2). n and m refer to the wave numbers of the STF and SLF, respectively. The pycnostat column shows the target values used in Eq. (18). For ρ_μ^0, μ indicates the wave number of the density component being controlled. The thermostat column shows the target values used for Eq. (17). $T_0^0 = 0.765$ for all simulations and is not displayed. A is a constant nonzero value used in the pycnostat for system 3b where we use $A = 0.16,0.24,0.40$.

System	F_0^t (STF)	n	F_0^l (SLF)	m	Pycnostat	Thermostat
1a	0.05,0.10, . . . ,1.0	1				
1b	0.05,0.10, . . . ,1.0	1				$T_2^0, T_4^0 = 0$
1c	0.05,0.10, . . . ,1.0	1			$\rho_2^0, \rho_4^0 = 0$	
1d	0.05,0.10, . . . ,1.0	1			$\rho_2^0, \rho_4^0 = 0$	$T_2^0, T_4^0 = 0$
2a	0.5	1	0.0,0.2,0.4, . . . ,3.0	2		
2b	0.5	1	0.0,0.2,0.4, . . . ,3.0	2	$\rho_4^0 = 0$	
2c	0.5	1	−3.0	2	$\rho_4^0 = 0$	
3a	0.1	1	0.0,2.0,4.0,6.0	10	$\rho_2^0, \rho_{20}^0 = 0$	
3b	0.05	1			$\rho_8^0, \rho_{12}^0 = A/2$, $\rho_{10}^0 = A$,	

[34,35] is used to solve for the time evolution of the system with a time step of 0.001.

Initially, each system is melted from a crystal state until it reaches an equilibrium fluid state with the above macroscopic state parameters. This transition occurs in less than 5×10^4 time steps. Once a system is in the equilibrium state we apply the external fields. The system evolves through a transient period before it reaches a desired steady state. We allow 1×10^5 time steps to ensure that the system is at steady state before production runs. For production runs we ensemble average over five or ten systems, each running for 2×10^6 time steps. By randomizing the initial momenta we ensure that each system in the ensemble average has a different microscopic state but the same macroscopic state.

A summary of all simulations performed in this paper is provided in Table I. We have simulated three systems, which are labeled and divided into subsystems. The thermostat and pycnostat columns display the target values that are used in Eqs. (17) and (18), respectively. The zero-wave-vector thermostat is used in all simulations and is therefore not displayed. For all simulations $T_0^0 = 0.765$. In system 3b the pycnostat produces the density inhomogeneities rather than the SLF and the constant A refers to the amplitude of the density perturbation.

IV. RESULTS

A. STF only: Long wavelength density perturbations

System 1 is an STF-only system. From Table I we can see that for all simulations in this paper we use an STF that has one full wave cycle over the simulation cell length l_y in the y direction. Thus, in all simulations Eq. (1) has $n = 1$, implying that $k_n = k_1 = 0.498$. For all system 1 simulations the STF field strength is the varying parameter, where we use the values $F_0^t = 0.05,0.10, \ldots ,1.0$. In the steady state for each value of F_0^t and with $n = 1$ we expect a velocity profile,

$$u_x(y) = u_1 \sin(k_1 y) + u_3 \sin(k_3 y) + u_5 \sin(k_5 y) + \cdots , \quad (21)$$

where we have dropped the subscript x from the Fourier velocity coefficient labels since we will only consider streaming flow in the x direction. The $u_3 \sin(k_3 y)$, $u_5 \sin(k_5 y)$, and higher terms represent the nonlinear velocity response. These higher harmonics are excited for larger field strengths. We have confirmed that for the STF field strengths used in these simulations, terms higher than u_5 are negligible.

For the velocity profile given in Eq. (21) the temperature profile is

$$T(y) = T_0 + T_2 \cos(k_2 y) + T_4 \cos(k_4 y) + \cdots , \quad (22)$$

and the density profile is

$$\rho(y) = \rho_0 + \rho_2 \cos(k_2 y) + \rho_4 \cos(k_4 y) + \cdots . \quad (23)$$

The density profile is mostly, but not entirely, due to thermal expansion caused by viscous heating, which is maximum where the velocity gradients are greatest. From simulation we are able to show that for increasing STF field strengths ρ_2 is proportional to T_2 and that ρ_4 is proportional to T_4 when neither the nonzero-wave-vector thermostat nor the pycnostat are being used. This proportionality is consistent with the equation of state. However, we find that when the pycnostat is used to maintain a homogeneous density profile only the T_4 component of the temperature series is suppressed (T_6 and higher terms are negligible). As we show in this section T_2 is reduced but not suppressed when the density is forced to be homogeneous. Likewise, reduced density inhomogeneities still form when the thermostat is used to eliminate kinetic temperature inhomogeneities. Therefore, as well as thermal expansion, other factors such as inhomogeneities in the configurational temperature or normal stress differences [36], must be involved in the relationship between the temperature and density profiles.

Figure 2 shows the velocity, density and temperature profiles for the set of system 1 simulations summarized in Table I. Results are shown for $F_0^t = 0.5$. The difference between systems 1a, 1b, 1c, and 1d is in the use of the pycnostat and thermostat. In system 1a (circles) we use neither the nonzero-wave-vector thermostat nor the pycnostat. Therefore, $\alpha_\upsilon = 0$ and $\beta_\mu = 0$ for all $\upsilon \neq 0$ and for all μ. In this way both the density and the temperature profiles are free to form naturally in response to the velocity gradients. In order to maintain steady state all excess heat generated by the STF is removed through the zero-wave-vector thermostat. In system 1b (triangles) we use the nonzero-wave-vector thermostat to

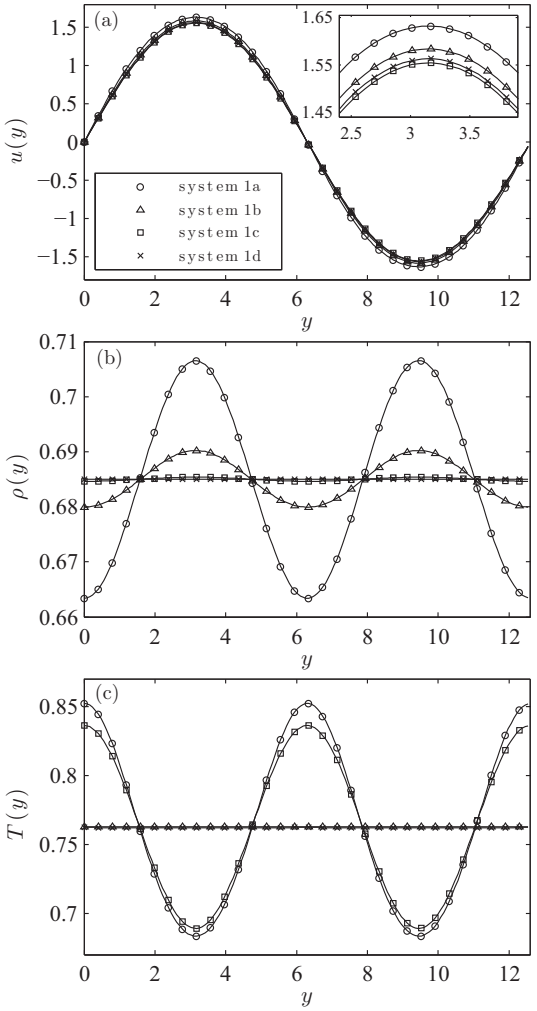

FIG. 2. (a) STF-induced velocity profiles, (b) density profiles, and (c) temperature profiles for different combinations of thermostat and pycnostat. All results shown are for $F_0^t = 0.5$ and $n = 1$ for the STF given in Eq. (1). All density and temperature inhomogeneities are shear induced.

eliminate all gradients in the kinetic temperature. For the calculation of $\dot{\alpha}_\upsilon$ in Eq. (17) we set $T_2^0 = 0$ and $T_4^0 = 0$. Equation (22) therefore reduces to $T(y) = T_0$. In system 1b no pycnostat is used. Systems 1a and 1b are similar to those described by Baranyai *et al.* [23], except that we are using different values for the system parameters such as N, F_0^t, ρ_0, and T_0. In systems 1c and 1d we introduce the cosine component pycnostat to suppress density inhomogeneities. Using Eq. (18) we set the feedback target values $\rho_2^0 = 0$ and $\rho_4^0 = 0$ in the calculation of β_2 and β_4, respectively. All higher-order terms are negligible. Thus, for suitably chosen values of ξ_υ we can reduce the density profile in Eq. (23) to $\rho(y) = \rho_0$. In system 1c (squares) we use the pycnostat to suppress density inhomogeneities but include no cosine component thermostats. Finally, in system 1d (crosses) we are simultaneously using the nonzero-wave-vector thermostat and the pycnostat such that we are suppressing both the temperature and density inhomogeneities.

In Fig. 2(a) we see that the various combinations of homogeneous and inhomogeneous density and temperature do not result in greatly different velocity profiles. We can see, however, from the inset, which is a magnification of the peak in the velocity profiles, that there are variations. For the fluid which has neither pycnostat nor thermostat included we have the greatest flow velocity, while those with homogeneous density have smaller amplitude velocity profiles. We will see later when we introduce the SLF that this is the expected result. Figures 2(b) and 2(c) show that there is a mutual support between the formation of the density and temperature profiles such that when both are unconstrained, i.e., $\alpha_\upsilon = 0$ and $\beta_\mu = 0$ for all $\upsilon \neq 0$ and for all μ, then both the density and the temperature profiles are larger than they would be if the other property were to be homogeneous in y. Thus, by suppressing the inhomogeneity in one we reduce the magnitude of the perturbation in the other. We note that in system 1c there is no contribution from the $T_4 \cos(k_4 y)$ term to the temperature profile, which is the result of eliminating the density inhomogeneities.

On close inspection we see that the density profile of system 1c has a very small perturbation about the equilibrium value, despite the application of the pycnostat. This is because the value used for the feedback constant in Eq. (18) for controlling $\rho_2 \cos(k_2 y)$ is equal to the value used in system 1d, which is $\xi_2 = 1 \times 10^{-3}$ for both systems. In the absence of the thermostat, the pycnostat must work harder to oppose the fluid's tendency to form density perturbations. Although this value of ξ_2 is sufficient to eliminate the density perturbation when the thermostat is also included, it is not sufficient when the thermostat is removed. We have found that a feedback coefficient value of $\xi_2 = 5 \times 10^{-5}$ suffices to eliminate the perturbation from the density profile but we have included these effects to illustrate the point. It should also be noted that when we decrease ξ_2 further to $\xi_2 = 1 \times 10^{-5}$, i.e., we increase the feedback strength slightly, our MD program integrator failed. Therefore, in order to suppress stronger perturbations it may be necessary to use smaller time steps for the MD integrator algorithm.

It should be emphasized that in system 1d we have produced a shearing fluid that is homogeneous in both temperature and density. In instances where an investigation has previously been limited to the small field regime in order to avoid the onset of inhomogeneities the pycnostat and thermostat can now be used to investigate the large field domain for homogeneous fluids, such as in the calculation of the nonlocal viscosity using the STF method [25].

Figure 3 shows various coefficients of the density and velocity profiles for the set of system 1 simulations as a function of STF field strength F_0^t. We are here interested in the relationships between the density and velocity gradients so the dependence of the temperature Fourier components on the STF field strength is not shown. Figure 3(a) shows the ρ_2 coefficients for the four different system 1 simulations and the ρ_4 components for system 1a and 1b, which are the two systems with no pycnostat. Systems 1c and 1d can be assumed to have $\rho_4 = 0$ for all field strengths. The inset is a magnification of the results which lie between -0.001 and 0. In the main graph of Fig. 3(a) the ρ_2 components for systems 1a and 1b, displayed using circles and triangles, respectively, clearly increase as a function of field strength. The inset shows that for large STF field strengths the ρ_4 coefficients for systems 1a and 1b

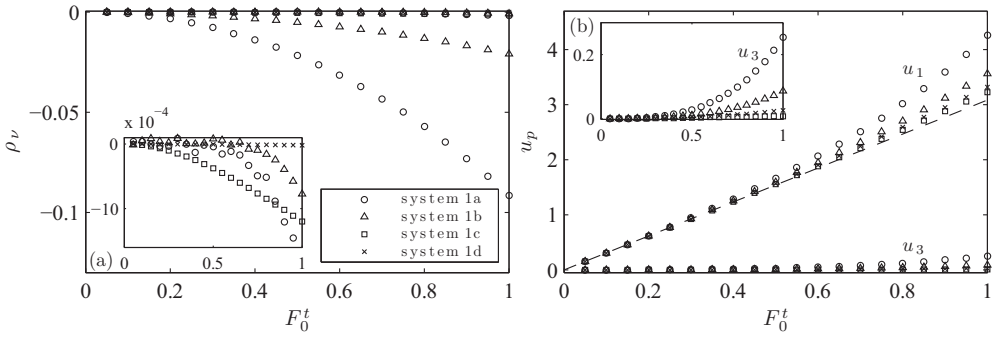

FIG. 3. (a) ρ_2 coefficients for the shear-induced density profile as a function of STF field strength. The inset is a magnification of the data that appears to be close to zero in the main graph. The ρ_4 coefficents for system 1a and 1c are also shown in the inset (dots and triangles, respectively). The circles and crosses in the inset are the ρ_2 coefficients for system 1b and 1d, respectively. (b) u_1 and u_3 coefficients for STF-induced velocity profile. The clusters of data points are labeled for each coefficient. The inset is a magnification of the u_3 data. The dashed line in the main graph is a linear extrapolation calculated using the first three data points from system 1b.

are also excited. Note that the values presented as the circles and triangles in the main graph (ρ_2 values) are different from the values presented by the circles and triangles in the inset (ρ_4 values). We use the same markers for ρ_2 and ρ_4 to indicate that the results are from the same system, where the order of magnitude can be used as a guide to distinguish which coefficient is being displayed. For large STF field strengths we excite higher-order harmonics in the density profiles for the nonpycnostatted systems. The behavior of the ρ_2 coefficients for systems 1c and 1d, which are the two systems with the pycnostat included, can be seen in the inset. The circles show the ρ_2 coefficient for system 1d, which has both pycnostat and Fourier component thermostat present. Clearly, in system 1d the pycnostat performs the function we expect by maintaining a zero value for the ρ_2 coefficient for all STF field strengths. Since we also apply the pycnostat to the ρ_4 component we assume it is also zero for all field strengths. The squares represent system 1c, which has the pycnostat present, but with no cosine component thermostat. Clearly, the pycnostat does not perform the function we expect from it. Again, these data have been included intentionally to illustrate a property of the feedback constant. Simulations with $\xi_2 = 5 \times 10^{-5}$ were also performed and we found that the increase of the ρ_2 coefficient with increasing field strength is greatly reduced.

For STF with $n = 1$ and for a density profile only including the average density and lowest-order perturbation term $\rho(y) = \rho_0 + \rho_2 \cos(k_2 y)$, which is true for small STF field strength, the equation for $P_{yx}(y)$ from Eq. (10) becomes

$$P_{yx}(y) = -\rho_0 \frac{F_0^t}{k_1} \cos(k_1 y) - \frac{\rho_2 F_0^t}{2k_1} \cos(k_1 y) - \frac{\rho_2 F_0^t}{2k_3} \cos(k_3 y). \quad (24)$$

We expect that when the density is homogeneous and the STF amplitude is small, the shear stress and strain rate should be related by the Newtonian constitutive relation $P_{yx}(y) = -\eta_0 \dot{\gamma}(y)$, where η_0 is the homogeneous shear viscosity. This is true if the wavelength of the STF field is significantly longer then the range of atomic interactions [19,20,25]. For inhomogeneous densities the viscosity will vary according to density. We discuss the local density dependent model briefly in Sec. IV C. When we use the pycnostat to suppress density inhomogeneities, in which case the second and third terms in Eq. (24) are negligible, we expect the velocity profile given by Eq. (21) to reduce to $u_x(y) = u_1 \sin(k_1 y)$. Figure 3(b) shows that this is almost, but not strictly, the case. The figure shows u_1 (upper curves) and u_3 (lower curves) for all of the simulations in system 1. The inset shows a magnification of the u_3 coefficients. The dashed line represents the extrapolation of a linear fit to u_1 vs F_0^t calculated from the first three data points of the system 1d data for u_1. We can see that in the presence of the pycnostat the dependence of u_1 on the field strength approaches the linear extrapolation. From the inset we can see that the u_3 coefficients are also greatly reduced. Thus, we must consider that for large field strengths there is an additional source of nonlinearity in the velocity profile that cannot be accounted for by inhomogeneous density.

We can compare our results with those obtained by Hansen *et al.* [25]. Using the u_1 coefficients for system 1a for the lowest seven field strength data points we assume that density inhomogeneities are negligible. Using Eqs. (24) and the Newtonian model we calculate the nonzero-wave-vector-dependent viscosity for $n = 1$ extrapolating to zero strain rate $\eta_{n=1} = \lim_{\dot{\gamma}\to 0} \rho_0 F_0^t / k_1^2 u_1$. We obtain a value of $\eta_{n=1} = 0.912 \pm 0.005$ using a least squares fit of a linear function to the data points. Using the parametrized Lorentzian function from Hansen *et al.* for the same ρ_0 and T_0 we can evaluate $\eta_{n=1} = 0.912 \pm 0.002$, where we have estimated their error bars at that data point. We can see that our results are in precise agreement.

B. Combined STF-SLF: Long wavelength density perturbations

Next we consider system 2 from Table I. We now keep the STF field strength fixed at $F_0^t = 0.5$ and introduce the SLF given in Eq. (2). We vary the SLF field strength over the range $F_0^l = 0.0, 0.2, 0.4, \ldots, 3.0$. We again set $n = 1$ for the STF and $m = 2$ for the SLF such that $k_m = k_2 = 0.996$. $\alpha_\upsilon = 0$ for all $\upsilon \neq 0$ so we can assume inhomogeneous temperature profiles. Equations (21) and (23) will again apply for the velocity and density profiles, respectively. In contrast to Sec. IV A we are now switching from observing the effect that controlling the velocity has on the density to observing the effect that controlling the density has on velocity. A visual representation of this system can be seen in Fig. 1.

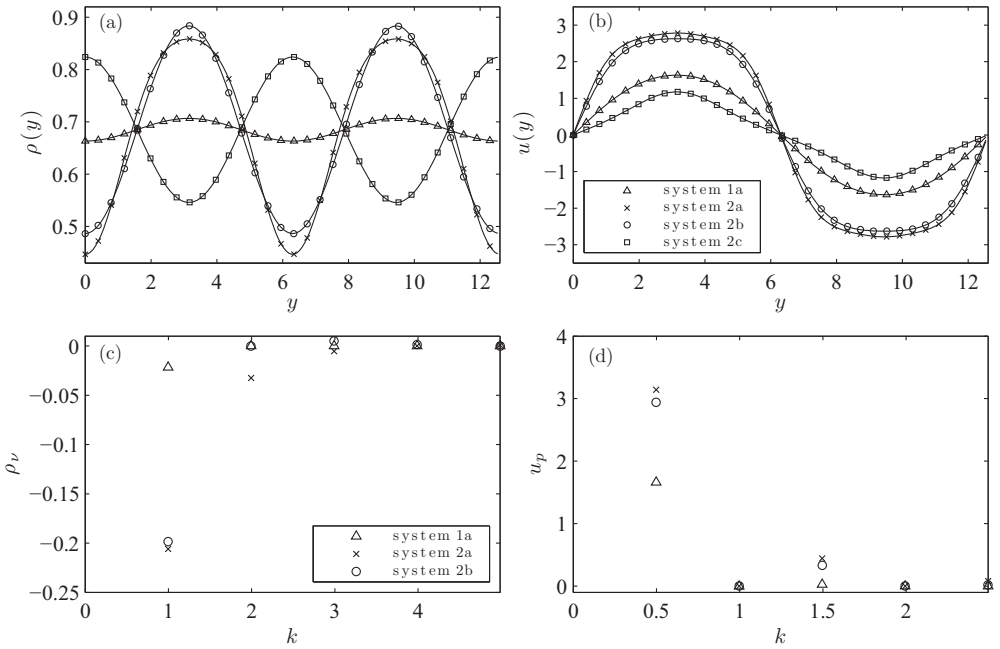

FIG. 4. Density and velocity profiles for combined STF-SLF system. STF field strength is $F_0^t = 0.5$ and $n = 1$. (a) y-space density profiles. Systems are defined in Table I. Triangles show the STF-only, shear-induced density. Crosses are for the combined STF-SLF with $m = 2$ and $F_0^l = 3.0$. There is no pycnostat so nonlinear density response components are included. Circles are for STF-SLF with nonlinear density response components suppressed using the pycnostat. Squares are for STF-SLF with $m = 2, F_0^l = -3.0$ and suppressed nonlinear density components. (b) y-space velocity profiles for fluid under the influence of the density profiles in (a). (c) Density coefficient spectrum showing $\rho_2, \rho_4, \rho_6, \rho_8, \rho_{10}$ for profiles in (a) ($F_0^l = -3.0$, system not shown). (d) Velocity coefficient spectrum showing u_1, u_3, u_5, u_7, u_9 for profiles in (b) ($F_0^l = -3.0$, system not shown).

For large field strength SLF, higher-order cosinusoidal harmonics are excited in the density profile [26]. In order to investigate the effects of density inhomogeneities in shear flow we might wish to apply single cosine component density perturbations. In this case the additional excited cosine density harmonics due to the nonlinear density response would be undesirable. Without the pycnostat we could only achieve this single cosine density component isolation by ensuring that we are in the linear density response regime. For the SLF external field with wave number approximately equal to or less than k_2 the linear response regime is typically satisfied for $F_0^l < 1$. Figure 4(a) shows four density profiles. The first is the density profile (triangles) induced by the STF-only system 1a described in Sec. IV A. The second density profile (crosses) is for system 2a in Table I for fixed value $F_0^l = 3.0$. There is no pycnostat present so the density profile is a cosine series with all nonlinear terms included. The third density profile (circles), which is for system 2b, has a pycnostat applied to all nonlinear components such that we maintain $\rho_4 = 0$ and $\rho_6 = 0$. Thus, at these high field strengths where the nonlinear response has been shown to be significant, we can use the pycnostat to ensure that only the lowest-order Fourier component is present. A k-space spectral plot of the first five cosine series density coefficients for Eq. (23), i.e., $(\rho_2, \rho_4, \rho_6, \rho_8, \rho_{10})$, is shown for these first three density profiles, confirming that only the single $\rho_2 \cos(k_2 y)$ component is present for system 2b. Simulations also confirm that the coefficients ρ_ν for all odd values of ν are zero.

Figure 4(b) shows the velocity profiles for the combined STF-SLF flow with $F_0^t = 0.5$ and the four density profiles shown in Fig. 4(a). Triangles show the velocity profile for $F_0^l = 0.0$. For the two cases where the SLF has field strength $F_0^l = 3.0$, i.e., when there are large density perturbations present, there is a large increase in the amplitude of the velocity profiles. Figure 4(d) shows the k-space spectral plot of the velocity profile. We can clearly see that the u_1 and u_3 components are much greater in the presence of large density perturbations. The SLF forces a greater number of atoms towards the peak regions of the STF field strength. Consequently, there is a reduction in the average density about the regions where STF field strength is zero ($y = 0$, $l_y/2$, and l_y). The STF is therefore doing more work on the system than it does when the density is homogeneous. The increase of energy input by the STF is manifested as an increase in streaming momentum in each streaming direction. Furthermore, the decrease in density in the regions where the flow changes direction will result in a decrease in energy dissipation. The maximum amplitude velocity profile occurs when the nonlinear density component is present (system 2a). From Fig. 4(a) we can see that the density minimum is least for this system. For system 2c (squares) we shift the phase of the SLF by half of a cycle by setting $F_0^l = -3.0$. Here the SLF forces the fluid to have density maxima in the regions where the STF is zero. We use the pycnostat to suppress the nonlinear density response components. Now the STF does less work on the system than it does when the density is homogeneous. There will also be greater dissipation of energy in the regions where the flow changes direction due to the greater density here. As we would expect, the velocity profile for system 2c in Fig. 4(b) shows a decrease in amplitude. The Fourier

TABLE II. Numerical values for the Fourier coefficients of the density and velocity profiles shown in Fig. 4.

	1a	2a	2b	2c
ρ_0	0.685	0.685	0.685	0.685
ρ_2	−0.022	−0.206	−0.198	0.139
ρ_4	0.000	−0.032	0.000	0.000
ρ_6	0.000	−0.005	0.005	0.001
u_1	1.662	3.143	2.938	1.043
u_3	0.029	0.442	0.332	−0.123
u_5	0.000	0.083	0.022	0.010

coefficient spectrum for system 2c has not been included in Figs. 4(c) and 4(d). Table II shows the numerical values for the density and velocity coefficients for all results in Fig. 4.

Figure 5(a) shows the Fourier coefficients for the linear and first nonlinear density response components as a function of SLF field strength for system 2a (triangles) and system 2b (circles). We can clearly see that for system 2b the pycnostat eliminates the nonlinear component ρ_4. Figure 5(b) shows the first three coefficients for the velocity series as a function of increasing SLF field strength. For fixed STF field strength $F_0^t = 0.5$ the velocity coefficients increase due to the increasing density perturbations. The inset shows a magnification of the u_3 and u_5 coefficients. Although the effect is only small we observe that the u_5 coefficient is excited for large density perturbations and that when the nonlinear density component is suppressed this higher-order effect does not completely disappear.

If we remove the pycnostat then for large field strength SLFs the series representation of P_{yx} will have contributions from the linear and lowest-order nonlinear density response components. We neglect any higher-order terms. Equation (10) therefore becomes

$$P_{yx}(y) = -\rho_0 \frac{F_0^t}{k_1}\cos(k_1 y) - \frac{\rho_2 F_0^t}{2k_1}\cos(k_1 y) - \frac{\rho_2 F_0^t}{2k_3}\cos(k_3 y) - \frac{\rho_4 F_0^t}{2k_3}\cos(k_3 y) - \frac{\rho_4 F_0^t}{2k_5}\cos(k_5 y). \quad (25)$$

TABLE III. Numerical values for the $P_{yx}(y)$ pressure tensor component corresponding to systems presented in Fig. 4. $F_0^t = 0.5$ and density coefficients are taken from Table II.

	1a	2a	2b	2c
$\rho_0 F_0^t/k_1$	0.687	0.687	0.687	0.687
$\rho_2 F_0^t/2k_1$	−0.011	−0.103	−0.099	0.069
$\rho_2 F_0^t/2k_3$	−0.004	−0.034	−0.033	0.023
$\rho_4 F_0^t/2k_3$	0.000	−0.005	0.000	0.000
$\rho_4 F_0^t/2k_5$	0.000	−0.003	0.000	0.000

Using the appropriate values from Table II we can evaluate each of the coefficients in Eq. (25) for the four systems described in Fig. 4. These values are presented in Table III.

Using Eq. (25) and the values in Table III we can plot the $P_{yx}(y)$ profiles for the four systems described in Fig. 5. This is done in Fig. 6. The triangles represent the STF-only system 1a. This system is characterized by a relatively small density perturbation. For this system there will be a small contribution from the second and third terms in Eq. (25). The fourth and fifth terms are negligible. The crosses represent $P_{yx}(y)$ for system 2a. The large density perturbation has the effect of reducing the amplitude of the shear stress profile. From Eq. (25) we can see that this is due to the interplay between the first two terms, both of which have wave number k_1. Since ρ_2 is negative the signs of these two terms are opposite. This reduces the contribution of this component to the total $P_{yx}(y)$. When we shift the phase of the density profile by using $F_0^l = -3.0$ in system 2c we change the sign of the second P_{yx} component in Eq. (24). This increases the total amplitude of the k_1 component. Using the pycnostat to suppress the nonlinear density response component produces a small effect in comparison to the order of magnitude of the total amplitude of P_{yx}. The amplitude of $P_{yx}(y)$ is greater when the $\rho_4\cos(k_4 y)$ density component is suppressed. This is the effect of the interplay between the third and fourth terms of Eq. (25), both of which have wave number k_3. Recall that the multiple appearance of terms with equivalent wave numbers in the P_{yx} series is due to our choice of n and m in Eqs. (1) and (2), respectively. A different wave number for the SLF, and hence density perturbation, would alter the terms present in Eq. (25).

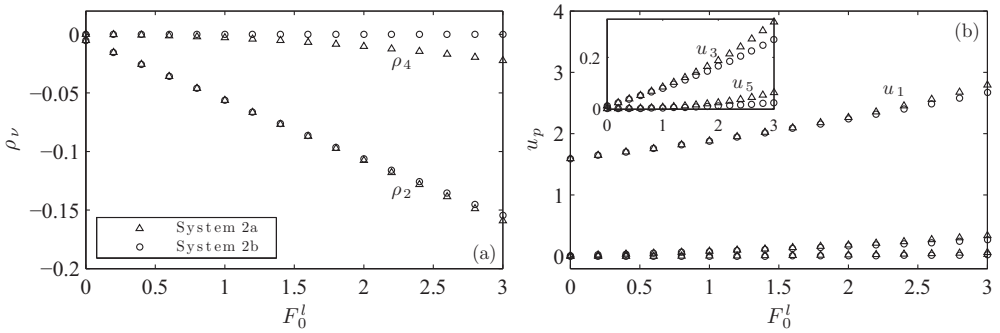

FIG. 5. Fourier coefficients of the density and velocity profiles under combined STF-SLF shown as a function of SLF field strength for $m = 2$ and fixed STF field strength $F_0^t = 0.5$ with $n = 1$. (a) ρ_2 and ρ_4 density coefficients. The labeled clusters indicate the coefficient. Triangles show that nonlinear density response components are free to form. Circles show that the pycnostat maintains $\rho_4 = 0$, eliminating the nonlinear response component. (b) Velocity coefficients showing how u_1, u_3, and u_5 vary with and without the pycnostat. The inset shows a magnification of u_3 and u_5 values.

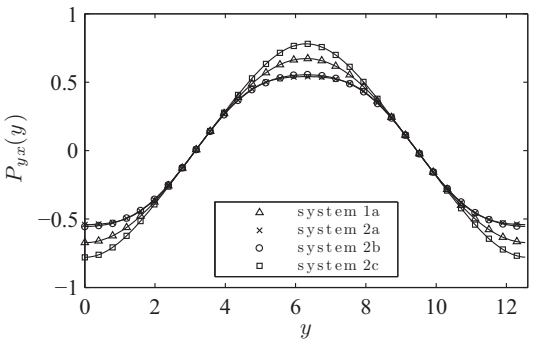

FIG. 6. $P_{yx}(y)$ constructed as a cosine series with coefficients in Table III, showing the $P_{yx}(y)$ profiles corresponding to the four systems shown in Fig. 4.

C. Combined STF-SLF: Short wavelength density perturbations

We now consider the effect of short wavelength density perturbations in shear flow. Figure 7 shows the density and velocity profile for a fluid under STF with $n = 1$ and SLF with $m = 10$ such that $k_m = k_{10} = 4.980$. This system is described in Table I as system 3a. For the STF we use $F_0^t = 0.1$. Results are shown for the set of SLF field strengths $F_0^l = 2.5$, 4.0, and 5.5. We have applied a pycnostat to the 2nd and 20th

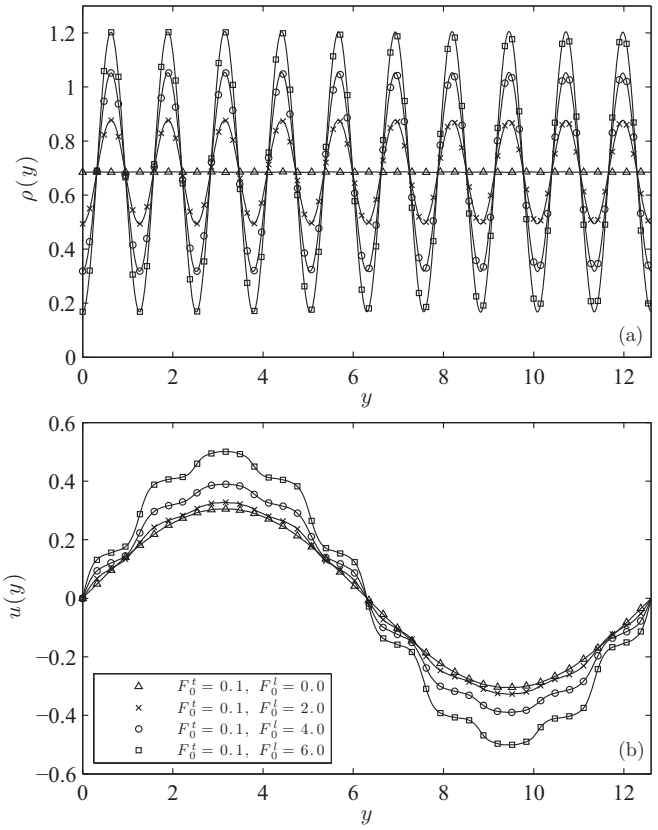

FIG. 7. (a) Density profiles produced using SLF with $m = 10$ for various field strengths. Triangles show the homogeneous density profile. The crosses, circles, and squares are for $F_0^l = 2.5$, 4.0, and 5.5, respectively. (b) Velocity profiles for systems under the influence of density profiles in (a). The STF field strength is fixed at $F_0^t = 0.1$ for all systems.

density cosine series terms such that $\rho_2 \cos(k_2 y) = 0$ and $\rho_{20} \cos(k_{20} y) = 0$. ρ_2 represents the shear-induced perturbation and ρ_{20} represents the lowest-order nonlinear response to the density perturbations in $\rho_{10} \cos(k_{10} y)$. We could equally have allowed these terms to appear but have chosen to present results for single component density perturbations. Only the zero-wave-vector thermostat has been employed so the temperature profile is inhomogeneous.

Figure 7(a) shows the density profiles for the short wavelength SLF. We have also included results for the case of $F_0^l = 0.0$. Figure 7(b) shows the corresponding velocity profiles. The effect of the density inhomogeneity on the velocity profiles is clear. As we introduce the density perturbations we see higher-order harmonics appear in the velocity profile. For the single wavelength density perturbations used in these simulations the additional velocity components are $u_9 \sin(k_9 y)$ and $u_{11} \sin(k_{11} y)$. There is also clearly an increase in the fundamental component. For larger density perturbations we can see the appearance of alternating regions of lesser and greater gradient in the velocity profile. The regions of lesser gradient in the velocity profile are aligned with periodic density maxima and the regions of greater gradient are aligned with density minima.

The SLF essentially confines atoms to planar layers that periodically divide the simulation cell normal to the y dimension. It does so by placing a corrugated potential energy field over the cell with cosinusoidally varying peaks and troughs, where for the conservative SLF the potential energy field ψ will be given by $\psi(y) = -\int F_y^l(y) dy = -F_0^l / k_m \cos(k_m y)$. For sufficiently large field amplitudes it is conceivable that atoms in any given potential minimum region will not have enough kinetic energy to overcome the potential energy barrier dividing neighboring regions. The STF does work on the atoms in each layer, accelerating them in the x direction. If we prevent dissipative interactions between neighboring layers by applying large SLF fields then the atoms in each layer will continue to accelerate in the x direction proportional to the STF field strength. In the extreme case of zero density at the minima, no steady state would be possible. From Fig. 7(a) we see that the density minima are greater than zero for all simulations. At these low densities, dissipative interactions are greatly reduced but are still occurring; therefore, we achieve a steady state. The regions of lesser gradient in the velocity profile are regions of density maxima and common streaming velocity with reduced viscous interaction between neighboring layers. Although the gradients are decreased the changes in the velocity profile still represent the varying STF field strengths across a given layer. The regions of greater velocity gradient correspond to potential energy maxima separating neighboring layers.

The density profiles that form in response to short wavelength SLFs have qualities analogous to the density profiles that form in nanoconfined fluids. In both cases the oscillations cycle over length scales of the order of single atomic diameters. For large amplitude SLF we can produce density variations comparable to those at the wall-fluid interface. In the case of the largest density perturbation in Fig. 7(a) the density minimum occurs at approximately $\rho_{\min} = 0.2$ and the maximum at approximately $\rho_{\max} = 1.15$. From Travis and Gubbins [2] we can see that the greatest peaks in the density for a confined fluid, which occur at the peak closest to the wall, have maximum values of anywhere between 0.9 to 1.3 for a mean

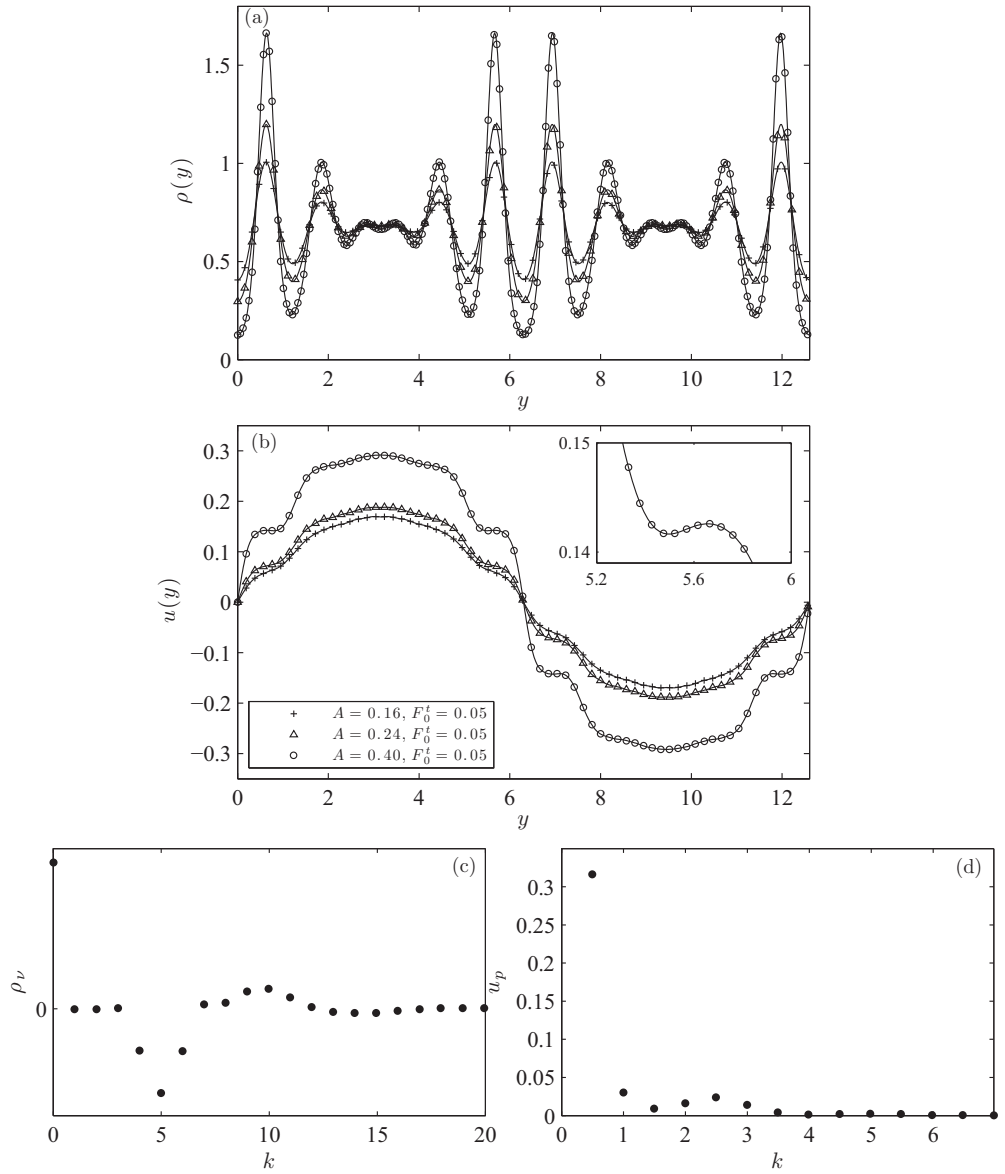

FIG. 8. (a) Density profiles produced using multiple cosine components Eq. (26). (b) Velocity profiles for systems under the influence of density profiles in (a). STF field strength of $F_0^t = 0.05$ is used for all systems with $n = 1$. The inset shows a magnification of one of the inflection points for the $A = 0.40$ system. (c) Density cosine series coefficient spectrum for $A = 0.40$ profile in (a) showing even ν terms. Nonlinear response components are represented by $N(y)$ in Eq. (26). (d) Velocity sine series coefficients for $A = 0.40$ profile in (b) showing odd p terms.

density of slightly lower than 0.75. For a confined fluid the minimum in the density closest to the wall necessarily goes to zero due to the excluded volume. The first minimum away from the wall has values between 0.4 and 0.6. From Todd *et al*. [3] we see a first peak maximum of around 1.57 and minimum of 0.53 for an average value of 0.8362, and a first peak maximum of 0.51 and minimum of 0.39 for an average value of 0.4181.

The most significant difference between the short wavelength SLF density and the confined fluid density is that for the confined fluid the density oscillations decay with increasing distance from the wall. For sufficiently large channel widths the oscillations will decay entirely and hence the center of a channel will have a region of homogeneous bulk density. We can extend the analogy between the SLF and nanoconfined fluid density by using a superposition of three suitably chosen cosine density components. The density profiles given by the following equation are shown in Fig. 8 for $A = 0.16$, 0.24, and 0.40:

$$\rho(y) = -\frac{A}{2}\cos(k_8 y) - A\cos(k_{10} y) - \frac{A}{2}\cos(k_{12} y) + N(y). \tag{26}$$

This system is referred to in Table I as system 3b. Since we require specific amplitudes for three cosine components we have used the pycnostat to produce the density profiles. We do so by setting the target values in the pycnostat feedback

equations Eq. (19) to $\rho_8^0, \rho_{12}^0 = A/2$ and $\rho_{10}^0 = A$. $N(y)$ in Eq. (26) represents all of the nonlinear response terms that we excite in the density due to the large fields employed by the pycnostat to maintain the three desired components.

The density profiles in Fig. 8(a) are symmetric about $l_y/2$. For the sake of our analogy to the confined system consider that each half of the density profile represents the density profile of a single *pseudochannel*. Each of the greatest peaks represents a peak that occurs closest to a wall-fluid interface, with the two adjacent peaks in the center of the profile each belonging to a different channel. The spectrum of the coefficients for the cosine series of the density profile is shown in Fig. 8(c) for $A = 0.40$. Only the cosine coefficients for k_ν with even values of ν are shown. We have confirmed that all terms with odd ν are zero. The three components that are being perturbed by the pycnostat are clearly visible at $k_8 = 4.486$, $k_{10} = 5.483$, and $k_{12} = 6.480$. The other nonzero components of the spectrum are due to nonlinear density response and are represented in Eq. (26) as $N(y)$.

It should be noted that by varying the cell dimension l_y one changes the wave numbers of periodic sine and cosine functions in the Fourier series. This means that, due to the k dependence of the nonlinear response, the nonlinear response terms included in $N(y)$ will be of greater or lesser sensitivity for different values of l_y. In many instances the nonlinear response will be of greater sensitivity and so higher-order terms will become more prominent in the total density profile. This may disturb the ideal channel-like form of the density profiles in Fig. 8(a). It is possible to use additional pycnostat terms to eliminate the nonlinear density response.

Figure 8(b) shows the velocity profiles for a fluid that is driven to flow under the influence of the density profiles in Fig. 8(a) using STF with field strength $F_0^t = 0.05$ and $n = 1$. Each half of the velocity field across l_y represents flow through one of the pseudochannels. In a macroconfined system the flow driven by a constant gravitational field along the confining channel has a quadratic velocity profile. In a nanoconfined system the velocity profile still has a dominant quadratic component, but there are other contributions to the velocity profile due to increased confinement [2–4]. Although our velocity profile is not fundamentally quadratic it is also zero at the boundaries, which we consider to be $y = 0, l_y/2$, and l_y, is symmetric about the velocity peak at the center of the pseudochannel, and is continuous. In this sense the analogy to flow in a confined system is valid. The spectrum for the coefficients of the sine series is given in Fig. 8(d).

The most striking feature of the velocity profiles in Fig. 8(b) is shown in the inset, which is a magnification of the velocity profile in the region of one of the greatest density peaks for $A = 0.4$. Not only does the velocity profile exhibit regions of lesser and greater gradient, but it also exhibits a slight gradient reversal. This gradient reversal is a significant characteristic of the velocity profiles of nanoconfined fluids [2]. It should also be noted that this characteristic is not present in Fig. 7, where the density perturbation has a simpler form.

Finally, we can calculate the $P_{yx}(y)$ profile for systems 3a and 3b. Figure 9 shows $P_{yx}(y)$ for the $F_0^t = 0.1$ and $F_0^l = 5.5$ system given in Fig. 7 (circles) and for the $F_0^t = 0.05$ and $A = 4.0$ system given in Fig. 8 (triangles). To calculate these

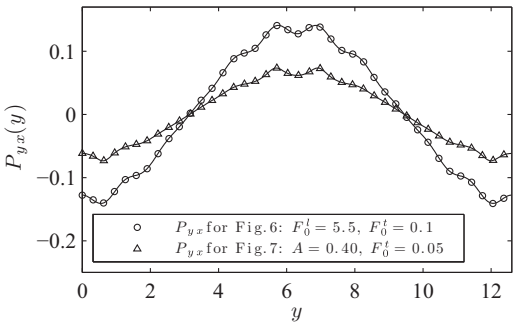

FIG. 9. $P_{yx}(y)$ profiles for $F_0^l = 5.5$ system presented in Fig. 7 and $A = 0.4$ system in Fig. 8. The profiles are a cosine series representation with coefficients determined using momentum balance equation Eq. (10).

profiles we use Eq. (10), which for the single component STF with $n = 1$ will reduce to

$$P_{yx}(y) = -\frac{\rho_0 F_0^t}{k_1}\cos(k_1 y) - \frac{F_0^t}{2}\sum_{\nu=1}^{\infty}\left[\frac{\rho_\nu \cos(k_{1+\nu} y)}{k_{1+\nu}} + \frac{\rho_\nu \cos(k_{|1-\nu|} y)}{k_{|1-\nu|}}\right], \tag{27}$$

where ρ_ν will be zero for all odd values of ν. Thus, the summation must extend over every cosine density component present in the density profile. For system 3a in Fig. 7 the only significant density component present is $\rho_{10}\cos(k_{10} y)$ since we have eliminated the shear-induced and nonlinear density response terms using the pycnostat. $P_{yx}(y)$ for system 3a is given by

$$P_{yx}(y) = -\frac{F_0^t \rho_0}{k_1}\cos(k_1 y) - \frac{F_0^t \rho_{10}}{2k_{11}}\cos(k_{11} y) - \frac{F_0^t \rho_{10}}{2k_9}\cos(k_9 y), \tag{28}$$

where $\rho_{10} = -0.483$.

For system 3b we can see from Fig. 8(c) that there are significant contributions to the density profile from many terms. To calculate $P_{yx}(y)$ we sum over all terms shown in the spectrum, where $\nu_{\max} = 40$. P_{yx} for system 3b (triangles in Fig. 9) is given by

$$P_{yx}(y) = -\frac{F_0^t \rho_0}{k_1}\cos(k_1 y) - \frac{F_0^t \rho_2}{k_3}\cos(2k_3 y) - \frac{F_0^t \rho_2}{2k_1}\cos(k_1 y) - \frac{F_0^t \rho_4}{k_5}\cos(2k_5 y) - \frac{F_0^t \rho_4}{2k_3}\cos(k_3 y) - \cdots - \frac{F_0^t \rho_{40}}{k_{41}}\cos(2k_{41} y) - \frac{F_0^t \rho_{40}}{2k_{39}}\cos(k_{39} y). \tag{29}$$

The large difference in the amplitude for the two $P_{yx}(y)$ profiles is due to the different STF amplitudes used for the two systems, which scale every term in the series. The fundamental component of each series provides the biggest contribution, with higher-order terms providing smaller variations to the

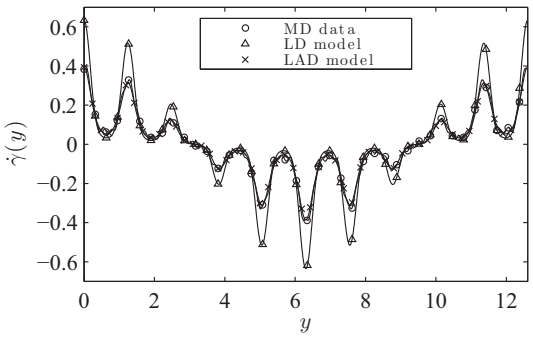

FIG. 10. Comparison between strain rate profiles for MD simulation data, the local density (LD) constitutive model, and the local average density (LAD) constitutive model, for $n = 1$, $m = 10$, and $F_0^l = 4.0$.

profile. Finally we note that since each coefficient in the series is inversely proportional to the wave number, the relative contributions of the terms decrease for shorter wavelengths.

If we consider just half of the P_{yx} profiles in Fig. 9, in the range between $y = 0$ and $l_y/2$, for example, then we can again compare the results obtained using the channel-like density profiles to those obtained for the confined flow. From Todd *et al.* [3] the $P_{yx}(y)$ profile observed for confined flow is fundamentally linear but with higher-order variations superimposed, especially in the regions near the wall where the oscillation in density is strongest. The linear component in the confined flow $P_{yx}(y)$ profile is due to the velocity profile being fundamentally quadratic. The gradient of the velocity profile will therefore be fundamentally linear. Since the velocity profiles in this paper are sinusoidal the velocity gradients are cosinusoidal. Therefore, our analogy to the confined system is limited in that the fundamental components of the $P_{yx}(y)$ profiles are different, but qualitatively similar.

As a final remark we briefly discuss the limitations of the local density constitutive relation. We used the set of values for the equal (ρ_0, T_0) state point from Hansen *et al.* [25] for homogeneous density-dependent viscosity and fit the data using a two parameter exponential function $\eta_0(\rho_0) = ae^{b\rho_0}$, where we calculate $a = 0.056$ and $b = 4.089$. Using this approximation to $\eta_0(\rho_0)$ and the P_{yx} profiles described in Secs. IV A, IV B, and IV C we can predict local density-dependent strain rate profiles, which we have compared with those directly measured using the MD simulations. We found that the local density-dependent viscosity accurately predicted the velocity profiles for the long wavelength density perturbations described in Secs. IV A and IV B for low field strength SLF. For larger SLF field strengths the predicted strain rate profiles began to deviate significantly from the MD profiles. Using the short wavelength SLF with $m = 10$; however, we were able to show that the local density model was less appropriate for predicting the strain rate. The deviation between the strain rate profile predicted by the local density model and the strain rate measured using MD was significant at smaller amplitudes in the density perturbation when we used a short wavelength SLF. Figure 10 shows the strain rate determined using MD and the strain rate predicted by the local density dependent viscosity model for $F_0^l = 4.0$ and $m = 10$. To improve the agreement between the prediction and the computed strain rate profile, we use the LADM, which matches very closely to the MD simulation results. For the LADM we use the simplest Bitsanis model [14], where the density is averaged with uniform weighting over a sphere. However, it is clear that the LADM cannot produce the regions of gradient reversal shown in the inset of Fig. 8(b). Therefore, a constitutive relation in which the shear stress is a nonlocal functional of both the strain rate and density may be required.

V. CONCLUSION

We have demonstrated a MD simulation method that uses a combination of two external fields to produce density and velocity inhomogeneities in an unconfined fluid under periodic boundary conditions. Although the method is synthetic, it is ideal for investigating the influence of nanoscale density inhomogeneities on shear flow due to the high level of control it provides over the velocity, density, and temperature profiles. This provides us with a greatly simplified method to investigate the relationship between strongly varying nanoscale density inhomogeneities and shearing velocity profiles when compared to the alternative approaches, such as the direct study of a realistic nanoconfined fluid.

We have not developed any new constitutive relations but have rather laid the foundations for their development by describing a rich and simple methodology for producing inhomogeneously shearing systems. It should be noted that this method can be applied to fluids of arbitrary complexity such as ionic fluids, polymeric fluids, and mixtures and can hence reveal characteristics that would be very difficult to isolate in simulations that mimic realistic nanoconfined systems. Any qualitative results obtained in the direct Fourier space treatment can be used in the development of a qualitative approach to the description of flow in a nanoconfinement geometry, and any constitutive relations determined using this proposed idealized system would also be valid for describing nanoconfined flow.

We showed that the shear-induced density variation is mostly due to thermal expansion caused by nonuniform viscous heating. However, when the thermostat and pycnostat constraints are used to suppress either one of the temperature or density inhomogeneities, respectively, then the inhomogeneities in the other property are not completely eliminated. This may be due to our decision to thermostat only the kinetic temperature or there may also be contributions to the density variations due to normal stress differences.

Using the SLF to perturb the fluid density normal to the direction of shear flow we were able to show systematically the excitation of higher sinusoidal modes in the velocity profile. We showed that the nonlinear velocity response was not entirely due to density inhomogeneities. When we completely suppressed the shear-induced density inhomogeneities in the STF-only system, the lowest-order term in the sinusoidal velocity profile still displayed a small nonlinear response and there was a slight excitation of the first higher-order term.

When the wavelength of the density perturbation is considerably less then the fundamental wavelength of the streaming velocity then the velocity profile exhibits short wavelength oscillations, which for large amplitude density perturbations appeared as very distinct inflections in the velocity profile.

Using carefully constructed density profiles with decaying amplitudes we were even able to produce gradient reversals in the velocity profile, which were observed by Travis and Gubbins [2] for nanoconfined flows.

We compared our results with those of Hansen *et al*. [25] and showed that we could reproduce the zero field strength extrapolation for the wave-vector-dependent viscosity. Using published data for the density dependence of the zero-wave-vector viscosity [25] we were able to show that for large amplitude or short wavelength density inhomogeneities the local density dependent constitutive model breaks down. The LADM was, however, suitable for describing the velocity gradients in these flows. In order to account for characteristics such as the gradient reversals in the velocity profile for a fluid that is strongly inhomogeneous in density over atomic length scales we would need to account for the nonlocal dependence of the shear stress on both the velocity gradient and the density inhomogeneity.

ACKNOWLEDGMENTS

B.D. would like to thank the Australian Nanotechnology Network (ANN) for their financial support and RMIT University for support through a postgraduate travel grant. He would also like to thank the Australian government for its support through the Australian Postgraduate Award and the Victorian Partnership of Advanced Computing for the use of their computer facilities. J.S.H. wishes to acknowledge the Lundbeckfoundation for supporting this work as a part of Grant No. R49-A5634. All authors would like to thank the Australian Research Council for supporting this project as part of the Discovery-Projects Scheme, Project No. DP120102976.

[1] I. K. Snook and D. Henderson, J. Chem. Phys. **68**, 2134 (1978).
[2] K. P. Travis and K. E. Gubbins, J. Chem. Phys. **112**, 1984 (2000).
[3] B. D. Todd, D. J. Evans, and P. J. Daivis, Phys. Rev. E **52**, 1627 (1995).
[4] K. P. Travis, B. D. Todd, and D. J. Evans, Phys. Rev. E **55**, 4288 (1997).
[5] H. T. Davis, J. Chem. Phys. **86**, 1474 (1986).
[6] H. T. Davis, Chem. Eng. Commun. **58**, 413 (1987).
[7] T. K. Vanderlick and H. T. Davis, J. Chem. Phys. **87**, 1791 (1987).
[8] L. Pozhar and K. E. Gubbins, J. Chem. Phys. **94**, 1367 (1991).
[9] L. Pozhar and K. E. Gubbins, J. Chem. Phys. **99**, 8970 (1993).
[10] L. A. Pozhar, Phys. Rev. E **61**, 1432 (2000).
[11] Z. Guo, T. S. Zhao, and Y. Shi, Phys. Rev. E **71**, 035301(R) (2005).
[12] Z. Guo, T. S. Zhao, and Y. Shi, Phys. Fluids **18**, 067107 (2006).
[13] U. M. B. Marconi and S. Melchionna, J. Phys.: Condens. Matter **22**, 364110 (2010).
[14] I. Bitsanis, J. J. Magda, M. Tirrell, and H. T. Davis, J. Chem. Phys. **87**, 1733 (1987).
[15] I. Bitsanis, T. K. Vanderlick, M. Tirrell, and H. T. Davis, J. Chem. Phys. **89**, 3152 (1988).
[16] H. Hoang and G. Galliero, J. Chem. Phys. **136**, 124902 (2012).
[17] H. Hoang and G. Galliero, Phys. Rev. E **86**, 021202 (2012).
[18] H. Hoang and G. Galliero, J. Phys.: Condens. Matter **25**, 485001 (2013).
[19] B. D. Todd and J. S. Hansen, Phys. Rev. E **78**, 051202 (2008).
[20] B. D. Todd, J. S. Hansen, and P. J. Daivis, Phys. Rev. Lett. **100**, 195901 (2008).
[21] P. J. Cadusch, B. D. Todd, J. Zhang, and P. J. Daivis, J. Phys. A: Math. Theor. **41**, 035501 (2008).
[22] E. M. Gosling, I. R. McDonald, and K. Singer, Mol. Phys. **26**, 1475 (1973).
[23] A. Baranyai, D. J. Evans, and P. J. Daivis, Phys. Rev. A **46**, 7593 (1992).
[24] K. P. Travis, D. J. Searles, and D. J. Evans, Mol. Phys. **97**, 415 (1999).
[25] J. S. Hansen, P. J. Daivis, K. P. Travis, and B. D. Todd, Phys. Rev. E **76**, 041121 (2007).
[26] B. A. Dalton, K. S. Glavatskiy, P. J. Daivis, B. D. Todd, and I. K. Snook, J. Chem. Phys. **139**, 044510 (2013).
[27] D. J. Evans and G. Morriss, *Statistical Mechanics of Nonequilibrium Liquids*, 2nd ed. (Cambridge University Press, Cambridge, UK, 2008).
[28] S. Nosé, Mol. Phys. **52**, 255 (1984).
[29] S. Nosé, J. Chem. Phys. **81**, 511 (1984).
[30] W. G. Hoover, Phys. Rev. A **31**, 1695 (1985).
[31] H. J. C. Berendsen, J. P. M. Postma, W. F. van Gunsteren, A. DiNola, and J. Haak, J. Chem. Phys. **81**, 3684 (1984).
[32] B. D. Todd and P. J. Daivis, Mol. Sim. **33**, 189 (2007).
[33] J. D. Weeks, D. Chandler, and H. C. Andersen, J. Chem. Phys. **54**, 5237 (1971).
[34] C. W. Gear, Math. Comput. **21**, 146 (1967).
[35] M. P. Allen and D. J. Tildesley, *Computer Simulation of Liquids*, 1st ed. (Clarendon Press, Oxford, UK, 1987).
[36] P. J. Daivis, B. A. Dalton, and T. Morishita, Phys. Rev. E **86**, 056707 (2012).